NeuroImage 283 (2023) 120430

Contents lists available at ScienceDirect

NeuroImage

journal homepage: www.elsevier.com/locate/ynimg

Reduced dimension stimulus decoding and column-based modeling reveal architectural differences of primary somatosensory finger maps between younger and older adults

Avinash Kalyani [a,b,*], Oliver Contier [c,d], Lisa Klemm [e,f,g], Elena Azañon [e,f,g], Stefanie Schreiber [b,g], Oliver Speck [b,e,f,h,i], Christoph Reichert [e,f,i], Esther Kuehn [a,b,f,j]

[a] Institute for Cognitive Neurology and Dementia Research (IKND), Otto-von-Guericke University Magdeburg, 39120, Germany
[b] German Center for Neurodegenerative Diseases (DZNE), Magdeburg, 39120, Germany
[c] Vision and Computational Cognition Group, Max Planck Institute for Human Cognitive and Brain Sciences, Leipzig, 04103, Germany
[d] Max Planck School of Cognition, Stephanstrasse 1a, Leipzig, 04103, Germany
[e] Leibniz Institute for Neurobiology (LIN), Otto-von-Guericke University Magdeburg, Germany
[f] Center for Behavioral Brain Sciences (CBBS) Magdeburg, Magdeburg, 39120, Germany
[g] Clinic for Neurology, Otto-von-Guericke University Magdeburg, 39120, Germany
[h] Department Biomedical Magnetic Resonance (BMMR), Otto-von-Guericke University Magdeburg, Germany
[i] Research Campus STIMULATE, Otto von Guericke University, Magdeburg, Germany
[j] Hertie Institute for Clinical Brain Research, 72076 Tübingen, Germany

ARTICLE INFO

Keywords:
Lifespan, sensory cortex
Decoding
Dimensionality reduction
UHF-MRI

ABSTRACT

The primary somatosensory cortex (SI) contains fine-grained tactile representations of the body, arranged in an orderly fashion. The use of ultra-high resolution fMRI data to detect group differences, for example between younger and older adults' SI maps, is challenging, because group alignment often does not preserve the high spatial detail of the data. Here, we use robust-shared response modeling (rSRM) that allows group analyses by mapping individual stimulus-driven responses to a lower dimensional shared feature space, to detect age-related differences in tactile representations between younger and older adults using 7T-fMRI data. Using this method, we show that finger representations are more precise in Brodmann-Area (BA) 3b and BA1 compared to BA2 and motor areas, and that this hierarchical processing is preserved across age groups. By combining rSRM with column-based decoding (C-SRM), we further show that the number of columns that optimally describes finger maps in SI is higher in younger compared to older adults in BA1, indicating a greater columnar size in older adults' SI. Taken together, we conclude that rSRM is suitable for finding fine-grained group differences in ultra-high resolution fMRI data, and we provide first evidence that the columnar architecture in SI changes with increasing age.

1. Introduction

Data aggregation is vital to increase the statistical power of analyses across individuals with varying functional topographies (Dervin, 1990; Mazziotta et al., 2001). For example, whereas differences in the functional topography of the hand area in sensory cortex between younger and older adults are almost impossible to detect at the single-subject level, group analyses allow detecting reliable and consistent differences across age groups (Liu et al., 2021). The study of multiple subjects is therefore crucial to comment on the significance of functional response differences generated in response to a common stimulus. A common problem, however, is inter-subject data alignment, particularly of ultra-high-field magnetic resonance imaging (UHF-MRI) data at a field strength of 7 Tesla (T) or above, where detailed features are encoded in a much higher spatial resolution, which sometimes does not align with the features used for anatomical alignment. Precise alignment is needed, however, to compare different age groups, patients against controls, or investigate changes across different time points in the course of learning or aging.

Functional and anatomical inter-subject alignment are two methods

* Corresponding author at: Institute for Cognitive Neurology and Dementia Research (IKND), Otto-von-Guericke University Magdeburg, 39120, Germany
E-mail address: avinash.kalyani@med.ovgu.de (A. Kalyani).

https://doi.org/10.1016/j.neuroimage.2023.120430
Received 31 January 2023; Received in revised form 28 September 2023; Accepted 25 October 2023
Available online 3 November 2023

to create a common analysis space (Sabuncu et al., 2010). The anatomical alignment uses anatomical landmarks, such as gyri or sulci, to create a common anatomical template (Brett et al., 2002; Fischl et al., 1999). However, the functionally defined regions are not necessarily consistent with these anatomical landmarks. For example, the location of the area related to visual motion perception (area MT) can show a variation of around 2 cm after anatomical normalization (Sabuncu et al., 2010). There are different reasons why anatomical normalization often fails to capture the fine-grained functional differences between individuals' brains, in particular, when UHF-MRI data is used: On one hand, smoothing across individuals is required as a step of normalization, and on the other hand, anatomical landmarks may not coincide with the structure of functional circuits (Guntupalli et al., 2016), making it inefficient for UHF-MRI inter-subject analysis.

Functional magnetic resonance imaging (fMRI) data is complex in nature. If every voxel represents a dimension of variation, the activity patterns over these voxels can be described as data points in a high dimensional space. The large number of voxels and the smaller number of volumes (TRs or time points) makes the high dimensional space sparse by nature, due to which statistical analyses are difficult and underpowered. Shared response modeling (SRM) (Chen et al., 2015) is a possible solution for the problems outlined above because SRM projects the fMRI time series of each participant to a low-dimensional space, which captures the temporal variance shared across subjects when exposed to the same stimulus or task sequence (for example: watching a movie (Häusler and Hanke, 2021)). The experimental manipulation or stimulus induces a series of cognitive or sensory states, like visual, auditory, or semantic, and shared variance is used to highlight the common variance related to these specific states between subjects. SRM, therefore, improves the statistical power by functionally aligning fine-grained spatial patterns in the specific region of interest (Cohen et al., 2017). Robust shared response modeling (rSRM) (Turek et al., 2018) is another such technique inspired by SRM and robust principal component analysis, which captures shared and individual components of brain activity across subjects. Even though this technique has great potential to solve common problems in UHF-MRI analyses, it has rarely been used for this purpose so far. Another similar technique that improves the alignment of fMRI time series across subjects is hyperalignment (Guntupalli et al., 2016, Feilong et al., 2021, 2018). It uses a Procrustean transformation to align the activity pattern across individuals into a higher dimensional common model space. For example, Kilmarx et al. (2021) used hyperalignment to align functional time series across individuals corresponding to finger presses, and then performed leave-one-subject-out classification. They found a significant improvement in classification accuracy ($p < 0.001$) of individual finger presses when group data was aligned based on function (88 %) rather than anatomy (46 %).

In a similar study by Al-Wasity et al. (2020), the authors successfully predicted imagined arm movements in the motor cortex using techniques of hyperalignment. While both studies involved sensorimotor tasks specific to digits and hands, in the present work, we focus on the fine-grained activity patterns evoked by passive touch in both younger and older adults. To reach this goal, we acquired high-resolution fMRI with an isotropic resolution of 1 mm at a 7 Tesla MRI scanner while participants were passively stimulated at their fingers using a Piezoelectric module.

We focus on tactile maps in the primary somatosensory cortex (SI) as a model system, whereas our outlined analysis approaches can also be applied to other brain areas or functional units. SI encodes tactile input to the skin in multiple subregions, in particular Brodmann Area (BA)1, BA2, and BA3b. Prior studies have shown that the topographic architecture in somatosensory representations differs in these subareas (Cassady et al., 2020). In addition, higher representational overlap is expected in older adults' compared to younger adults' topographic maps (Cabeza, 2002; Liu et al., 2021). However, in most studies, either 3T-fMRI data was used, or when 7T-fMRI data was used, functional features such as overlap or representational similarity were first extracted at the individual subject level and then averaged across the group, preventing voxel-wise analyses across the group (Liu et al., 2021).

A further open aspect about the functional organization of SI in younger versus older adults is its columnar architecture. Due to recent advances in fMRI techniques, we can now measure highly sensitive and spatially accurate signals, making it possible to study fundamental computational units (Yacoub et al., 2008) such as cortical columns. Two good examples of such a functional columnar organization in the brain that have already been studied using fMRI are the orientation columns in the primary visual cortex (V1) (Erwin et al., 1995), and fine-grained movement-dependent finger maps in the primary motor cortex (MI) (Huber et al., 2017, 2020, see Kuehn and Pleger, 2020 for review). For SI, it is unclear whether or not such columnar analyses can be used to describe the system, which columnar size would best represent SI finger maps, and whether columnar sizes would differ between younger and older adults. The question of whether or not columnar sizes differ with age is an aspect that has generally not received much attention in the literature so far. Please note that the term 'columnar' here refers to the mesoscopic structures aligned perpendicular (radial) to the cortical depths as defined based on cortex anatomy (Huber et al., 2020) where functional signals are then averaged per unit (i.e., column).

Here, we use rSRM to obtain information about the functional architecture of sensory finger representations in the SI of younger and older adults in response to passive tactile stimulation of the fingertips. More specifically, we investigate decoding sensitivity for finger discrimination across different BAs (BA3b, BA1, BA2) in SI as well as across the motor system (BA4a, BA4p, BA6), and compare them between younger and older adults. Then, we introduce a column-driven rSRM approach where the number of columns is varied as a hyperparameter to differentiate the tactile stimulation of fingers. In addition, we test whether this hyperparameter varies across age groups. Using the same principle of columnar mapping as introduced above, we then investigate the computational units in SI to determine the optimal columnar scale to describe finger representations in columnar units in younger and older adults. We argue that this method can in the future be also applied to other brain areas to determine the optimal columnar size within which functional maps can be described (for example in parietal cortex, insula, and hippocampus). The columns we describe here may represent the smallest unit of functional processing, i.e., population receptive fields. Note that the smallest unit that can be modelled is of course restricted by the measured voxel size, here 1 mm isotropic. We argue that the set of techniques we offer here provides key information about the architecture of SI, and is particularly useful for analyzing UHF-MRI data where the preservation of the individual information and spatial resolution is a key challenge.

2. Methods

2.1. Subjects

We tested n = 19 younger adults (mean age 25 ± 0.49, ranging from 21 to 29 years, number of females = 9) and n = 19 older adults (mean age 72.2 ± 0.81, ranging from 65 to 78 years, number of females = 9). Participants were recruited from the database of the Deutsches Zentrum für Neurodegenerative Erkrankungen (DZNE), Magdeburg, Germany. They were all healthy and were checked for 7T-MRI exclusion criteria, such as metallic implants and other foreign bodies, active implants (e.g. pacemaker, neurostimulator, cochlear implant, defibrillator, and pump system), permanent makeup, tinnitus, or other hearing impairments. The functional 7T-MRI scan was performed in a single session alongside a whole-brain MP2RAGE sequence. One additional 3T-MRI session took place on a separate day (see below). All participants were compensated for their time and attendance, and a written informed consent form was signed by the participants before each scan. The study was approved by

the Ethics Committee of the Otto-von-Guericke University Magdeburg. Parts of the data used here were also used by a recent paper that focused on population receptive field mapping (Liu et al., 2021).

2.2. Dataset and experimental design

2.2.1. MRI scanning

UHF-MRI data were recorded at a whole-body 7 Tesla Siemens MRI scanner in Magdeburg (Siemens Healthcare, Erlangen, Germany) using a 32 channel Nova Medical head coil. First, a whole-brain MP2RAGE sequence with the following parameters was acquired: Voxel resolution: 0.7 mm isotropic, 240 slices, FoV read: 224 mm, TR = 4800 ms, TE = 2.01 ms, TI1/2 = 900/2750 m, GRAPPA 2, sagittal orientation. Before acquiring the functional scans, shimming was performed and two volumes using echo-planar imaging (EPI) with opposite phase-encoding (PE) polarity were acquired. Then, functional gradient-echo (GE) EPI sequences with the following parameters were acquired: Voxel resolution: 1 mm isotropic, FoV read: 192 mm, TR = 2000 ms, TE = 22 ms, GRAPPA 4, interleaved acquisition, 36 slices. The same sequence was used for all functional tasks (see below). 3T-MRI data were acquired on a separate day at a Philips 3T Achieva dStream MRI scanner (at the in-house facility at the Leibniz Institute for Neurobiology (LIN)), where a standard structural 3D MPRAGE was acquired (resolution: 1.0 mm x 1.0 mm x 1.0 mm, TI = 650 ms, echo spacing = 6.6 ms, TE = 3.93 ms, flip-angle= 10°, bandwidth = 130 Hz/pixel, FOV = 256 mm×240 mm, slab thickness = 192 mm, 128 slices).

2.2.2. Stimuli and design

Participants were stimulated on their individual digits using a piezoelectric stimulator (Quaerosys, Schotten, Germany). We used five MR-compatible and independently controlled piezoelectric modules for tactile stimulation to the right hand's D1-D5, where D1 corresponds to the thumb, D2 to the index finger, D3 to the middle finger, D4 to the ring finger, and D5 to the little finger of younger and older adults. Stimulation was applied while they were lying in the 7T-MRI scanner. Each finger was attached to one module using a metal-free, custom-build applicator that could be easily adjusted to different hand and finger sizes (i.e., each module could be independently moved within the applicator until the pins in the stimulator were positioned under each fingertip). The stimulator (see Fig. 1A) had 8 pins arranged in a 2 × 4 array in the proximo-distal axis of the finger, covering a skin area of 2.5 × 9 mm^2. The vibrotactile stimulation was applied to the fingertips at a frequency of 16 Hz with only two pins rising at a given time to prevent adaptation (Schweizer et al., 2001). The frequency was a continuous sinusoidal function with the intensity adjusted to 2.5 times the individual tactile detection threshold for each subject and finger. Tactile detection thresholds were acquired on a separate day before scanning. The mean detection threshold used for older adults was 1.37 ± 0.07 g, and for younger adults, it was 0.80 ± 0.04 g (Liu et al., 2021).

There were two cyclic runs and, consecutively, two random-design runs. The cyclic runs consisted of 2 runs of 20 cycles each, with a duration of 25.6 seconds per cycle. On each run, each fingertip received stimulation for 5.12 seconds and was repeated 20 times. There was no delay between the end of one stimulation on one finger and the start of the next at a different finger. For each run, the stimulation was applied either in forward (D1 to D5) or reverse (D5 to D1) order. Forward and reverse orders were randomized across subjects and age groups (i.e., half of the subjects of each age group, and of each gender started with a forward run). Each run consisted of 256 scans (512 sec for TR = 2 seconds) and lasted for 8 minutes and 31 seconds with the same number of intervals in each run (15 in total). There was 1-minute rest between runs and no gap between repetitions. The order, forward (D1 to D5) or reverse (D5 to D1) order was chosen because cyclic designs have been found to be superior in sensitivity to detect precise topographic finger maps in area 3b (Kassraian et al., 2022; Kuehn et al., 2018).

For the random-design that was used as a localizer, there were 6 conditions: Stimulation to D1, D2, D3, D4, D5, and a rest condition. The stimulation protocol was similar to the cyclic design, i.e. each finger was stimulated for 5.12 seconds with the same frequency and intensity as described above. In contrast to the cyclic design, the order of finger stimulation was in a pseudo-random order, which was randomized in a way that no finger was stimulated more than twice in a row. There was a 2 seconds rest in 70 % of the trials and a 6 seconds rest in the remaining 30 % between every two subsequent stimulations. Every finger was stimulated 10 times. Each run comprised 210 scans, which lasted for 6 min and 56 sec. The random-design paradigm was repeated twice as well. The cyclic runs were used for the analyses using rSRM, whereas the random-design runs were used as a localizer for defining the ROI. Random designs are suitable as localizers because they are not biased by stimulation order (Kassraian et al., 2022). We note that in addition to the cyclic (D1 -> D5, D5 -> D1) and the random design, it would have been beneficial to also measure a cyclic design with a fixed but different stimulation order (for example D1, D3, D5, D2, D4) to control for order effects in the cyclic design analyses. However, the already long scanning time did not allow us to include more functional blocks into the scanning.

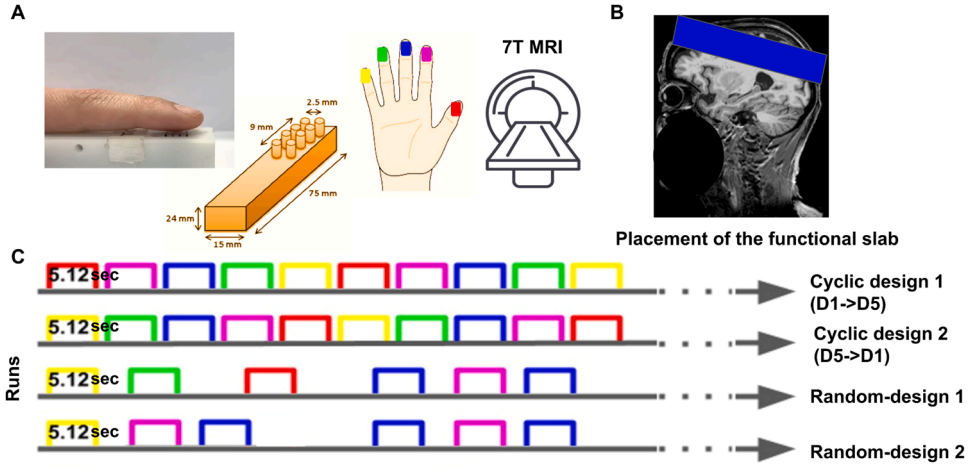

Fig. 1. Experimental design. Within the 7T-MRI scanner, a piezoelectric stimulator (see **A**) was used for fingertip stimulation. **B:** The blue area shows the placement of the slab image at an example participant's T1-weighted image. **C:** Each row represents one run with the first two rows representing cyclic-designs (Forward: D1 to D5, Reverse: D5 to D1) and the last two rows representing random-designs (each row represents one run). Each colour represents one finger of the right hand (colour code in **A**).

During both cyclic and random-design runs, there were small gaps of 180 ms inserted into the 5.12 seconds stimulation intervals to motivate subjects to focus on the stimulation (Schweisfurth et al., 2014). These gaps were randomly inserted within one stimulation block. It was the task of the participant in all 4 runs to count the number of gaps throughout the block and to verbally report the number after the block was finished. Gaps were pseudo-randomized in a way that each finger received the same number of gaps throughout the experiment. Counting the gaps ensured high attention of the participants towards the stimulus.

2.3. Preprocessing

Functional MR data acquired at a 7T MRI scanner can be corrupted by motion artifacts and geometric distortions due to participant movement and field inhomogeneity. To counter distortions, two opposite PE polarity EPIs were acquired prior to the functional scan. To perform distortion correction of both EPIs with opposite PE polarity, a point spread function (PSF) mapping method was applied (In et al., 2016). A weighted combination of the two distortion-corrected images was incorporated to maximize the spatial information content of the final corrected image, because the amount of spatial information differs between the opposite PE datasets. The EPI-images of the functional blocks were motion corrected to time point $t_0 = 0$, and the extended PSF method was applied to the acquired and motion-corrected images to perform geometrically accurate image reconstruction. This was followed by slice-timing correction using SPM8 (Statistical Parametric Mapping, Wellcome Department of Imaging Neuroscience, University College London, UK).

2.4. Decoding analyses

The 1st level fixed-effects models were computed separately for every participant using the general linear model (GLM) implemented in SPM8. This analysis was performed on the two random-design runs (see Fig. 1C). We modeled five regressors, one per digit (D1, D2, D3, D4, D5 stimulation). Then, five linear contrast estimates were computed (e.g. contrast [4 -1 -1 -1 -1] for touch to D1). No group alignment was performed; therefore, the anatomical and functional data were neither smoothed nor normalized. It is important to note that acquiring a separate dataset as a localizer allowed us to have independent datasets for defining the ROIs (i.e., the fingers) and training the rSRM. Using a random-design with randomized stimulation sequences allowed an optimal localization of each individual finger in each participant. The cyclic design was chosen for the rSRM, because the model requires the stimulation order to be the same for each participant. We chose a design where the stimulation order of the fingers matched the assumed representation order in S1. Using one forward- and one backward-run ensured that we controlled for effects of stimulation order. Therefore, for the first analysis scheme (see Section 3.2 for more details), the independently acquired random-design data was used as a localizer (i.e., for masking the top n-number [500, 1000, 1500, 2000, 2500, 3000] of significant voxels) that were used for the decoding of the cyclic data.

For the region of interest (ROI) based analysis scheme, the focus was on investigating the representations in different BAs, more precisely, to investigate seven BAs covering the sensorimotor system (BA1, BA2, BA3a, BA3b, BA4a, BA4p, BA6) in the hemisphere contralateral to the stimulation (i.e., right-hand stimulation, left hemisphere), whereas the regions in the ipsilateral hemisphere were used as a control. Freesurfer-based parcellation (version-v6.0.0) was performed using the command "recon-all" on the T1 anatomical maps. Note that both the structural data (3T MPRAGE data) and the functional data (7T EPI) had the same resolution (i.e., 1 mm isotropic) and could therefore be mapped onto each other. In order to co-register the 7T functional and the 3T structural images, a function-to-structure manual rigid co-registration was performed using ITK-snap (version 3.8) and Advanced Normalization Tools (ANTs version 2.1). ITK-snap was used to generate a transformation matrix, which was used to transform the functional data using ANTs. Rigid co-registration was performed because there were no morphological differences between the reference and the source. To maintain homogeneity, the top 500 voxels were selected from each region to perform the analysis across age groups and across different brain regions. This number was selected based on the highest stimulus decoding accuracy obtained for 500 voxels as compared to the other numbers. For columnar-based analyses, we focused on the precise functional representation of the somatosensory finger maps that exist in BA1 and BA3b in the hemisphere contralateral to the stimulation (i.e, left hemisphere).

2.4.1. Robust Shared Response Modeling (rSRM) for digit and age classification in different BAs

2.4.1.1. Robust shared response modeling. The underlying concept of rSRM is to determine a shared, lower-dimensional representation of the stimulus-response across participants who were presented with the same stimulus during scanning (here synchronized finger stimulation) while also capturing the individual component of brain response. This individual component captures the individual variance that is not captured by the shared representation. rSRM can be used to detect differences between individuals and groups. In the next sections we describe the two different approaches in which the model is used to predict age groups and the stimulated digit from brain responses. In rSRM, each subject's data is described as the sum of the shared response $R \in \mathbb{R}^{K\times t}$ and subject specific mappings $W_i \in \mathbb{R}^{N\times K}$, $i = 1...m$, individual term $S_i \in \mathbb{R}^{N\times t}, i = 1...m$ (with K number of features, t scanned volumes, N number of voxels, and m subjects) i.e. $X_i \approx W_i R + S_i$ (see Turek et al., 2018) (see Fig. 2). The individual terms mainly contain information not represented in the shared space. This information is very useful if the individual variation between the subjects is very high. In the following sections, we have outlined our methodology and procedures for data aggregation, specifically focusing on digit and age group classification. The model also contains a regularization parameter '$\lambda_i^{'}$ which controls the sparsity of the individual term, by regulating the amount of data to be considered for shared and individual terms. For our analysis we used a default value of '1.0' for this parameter.

2.4.1.2. Digit classification. For digit classification, we followed a two-step process for shared response modeling and classification, employing a leave-one-subject-out procedure for both separately. First, we used the robust SRM (Turek et al., 2018) to estimate the shared response of all subjects except for the one left out (l) i.e., during the training phase a shared representation $R \in \mathbb{R}^{K\times t}$, subject specific bases $W_i \in \mathbb{R}^{N\times K}$, $i = \{1...m\} \neq l$ and individual terms $S_i \in \mathbb{R}^{N\times t}$, $i = \{1...m\} \neq l$ were learned using the data from the first of the two runs of the cyclic design. The aim of this step was to identify common neural response patterns across subjects using rSRM. Then, the held-out subject's bases W_l and the individual term S_l was estimated using the learned shared response as a template. The second run (i.e. the test run data of the cyclic design) was then transformed using the individual subjects' bases W_i. This resulted in a set of reduced dimensional transformed data $\widehat{R_i} \in \mathbb{R}^{K\times t}$, and new individual term $\widehat{S_i} \in \mathbb{R}^{N\times t}$, due to the individual variability present in the individual term, it cannot be directly compared among subjects as it resides within each subject's topographical space. Therefore, we discarded the individual term from our analysis. The transformed test run data of the test subject $\widehat{R_l}$ served as input for the classifier. This step was repeated for all the subjects across both runs, in a cross-validation way. After obtaining the transformed data using rSRM, we proceeded to the classification step. Here, we trained and tested a linear support vector machine (SVM) using the transformed reduced dimensional data from all the subjects in a leave-one-subject-out procedure, that was performed separately for the two age groups, ensuring that no data from that participant was included during shared response estimation. This

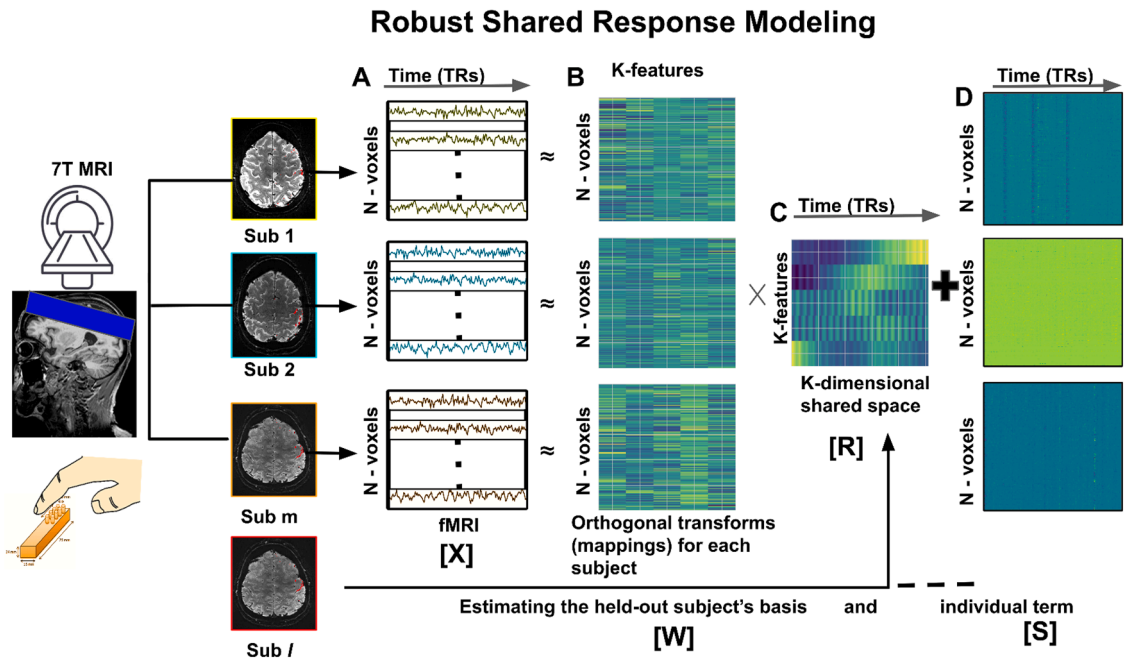

Fig. 2. Workflow of Robust Shared Response Modeling (rSRM). A: The model expects the same input for all subjects, which in our case was provided by a cyclic design (D1 -> D5 or D5 -> D1, see Fig. 1C for details). The matrix [X] represents the subject-wise and voxel-wise BOLD signal change. **B:** The matrix [W] with N voxels by *K* features is used for participant-specific mapping, and is also referred to as 'subject-specific basis' in the text. **C:** The model captures the underlying shared variance with *K*-dimensional shared space representation across subjects for all samples represented by matrix [R]. **D:** The matrix [S], refers to the subject specific individual term, this individual term contains information not captured by the shared space.

independent data evaluation guarantees that the classifier's performance is assessed on data that were not used for shared response modeling. We then computed the average accuracy and standard error by two-fold cross-validation across the two runs and leave-one-out over test subjects. In the classification task, we estimated if the shared response estimated by rSRM can be matched to the corresponding stimulated digit as the class label using a linear support vector machine (SVM) classifier in a one-vs-rest framework. We used the projected data of each scanned volume as training sample where the corresponding stimulated digit was set as class label, i.e. the feature space was *K*-dimensional. The achieved decoding accuracy we consider as an estimate of the alignment capability of rSRM using different selection methods of voxels (for BAs and columns, see Figs. 3A and 5D,E, respectively). Digit classification was carried out separately for the group of younger adults and the group of older adults (i.e., two leave-one-subject-out cross-validations were performed, see Figs. 3A, 4A). In the ROI based analysis BAs from the right and the left hemisphere were involved in the analysis with the right hemisphere as the control region for assessing the classification model (see Fig. 3A). The chance accuracy (i.e. Ac_{chance}) for this decoding analysis is 0.2, given 5 fingers were used for classification.

2.4.1.3. Age classification. For age classification, we employed two separate robust shared response models (rSRMs) to capture group-specific shared information, each with K number of features. We refer to these models as $rSRM_1$ and $rSRM_2$, corresponding to different age groups. Our goal was to create distinct shared spaces that capture the unique shared information for each age group. To achieve this, we trained $rSRM_1$ using the training run data from one age group, and $rSRM_2$ using the training run data from the other age group. This ensured that each shared space was optimized for the specific group it represents. Next, we utilized the test subject's train run data and estimated the basis and individual term separately for both $rSRM_1$ and $rSRM_2$'s shared feature space as templates. We then transformed the test run data of the test subject using the learned basis for both the age groups, the new estimated individual term was discarded at this step. This process resulted in two sets of projected data, corresponding to the younger and older age group rSRMs. These projected datasets were concatenated and served as the input data for the classifier. By doing so, we ensured that for a given subject, the classifier was trained on the feature sets considering projections to both the younger and older rSRMs. These steps were repeated for all the subjects one by one. In the classification step, the age group of the subjects served as the class label during classifier training and leave-one-subject out cross-validation. We repeated this process for all participants in both age groups, creating a comprehensive representation of the age groups in our dataset.

This approach effectively utilized the age group-specific shared information and enabled the classifier to make predictions on the subject's age group. In this analysis, we discarded the individual term to focus on capturing the group-specific shared information and remove the individual variability. It's important to note that the chance accuracy (Ac_{chance}) for this decoding analysis is 0.5, considering that we used two distinct age groups for classification. (see Fig. 4G, Fig. 3D).

2.4.2. Columnar-Shared Response Modeling (C-SRM)

Sensory and motor cortices can be divided into columnar units, which helps to detect fine-grained topographic maps with high precision (Huber et al., 2020; Yacoub et al., 2008; Yang et al., 2019). We here aim to identify the number of columns required to effectively decode the SI generated responses, i.e., the topographic representations triggered by passive tactile finger stimulation in younger and older adults. Note that because each finger was stimulated by 16 different combinations of pins (see Fig. 1A), the smallest computational unit may not be the representation of one finger but the representation of one or more pins touching the skin. We here focus only on the hemisphere contralateral to the stimulation (i.e., right hand stimulation, left hemisphere), and on the areas that offer a fine-grained representation of touch (i.e., BA1 and BA3b). First, we divide the two ROIs BA1 and BA3b into different numbers of columns (ranging from 10 to 400 approximately equi-volume columnar units, where the maximum number of possible columns is represented by voxel size) using the software package

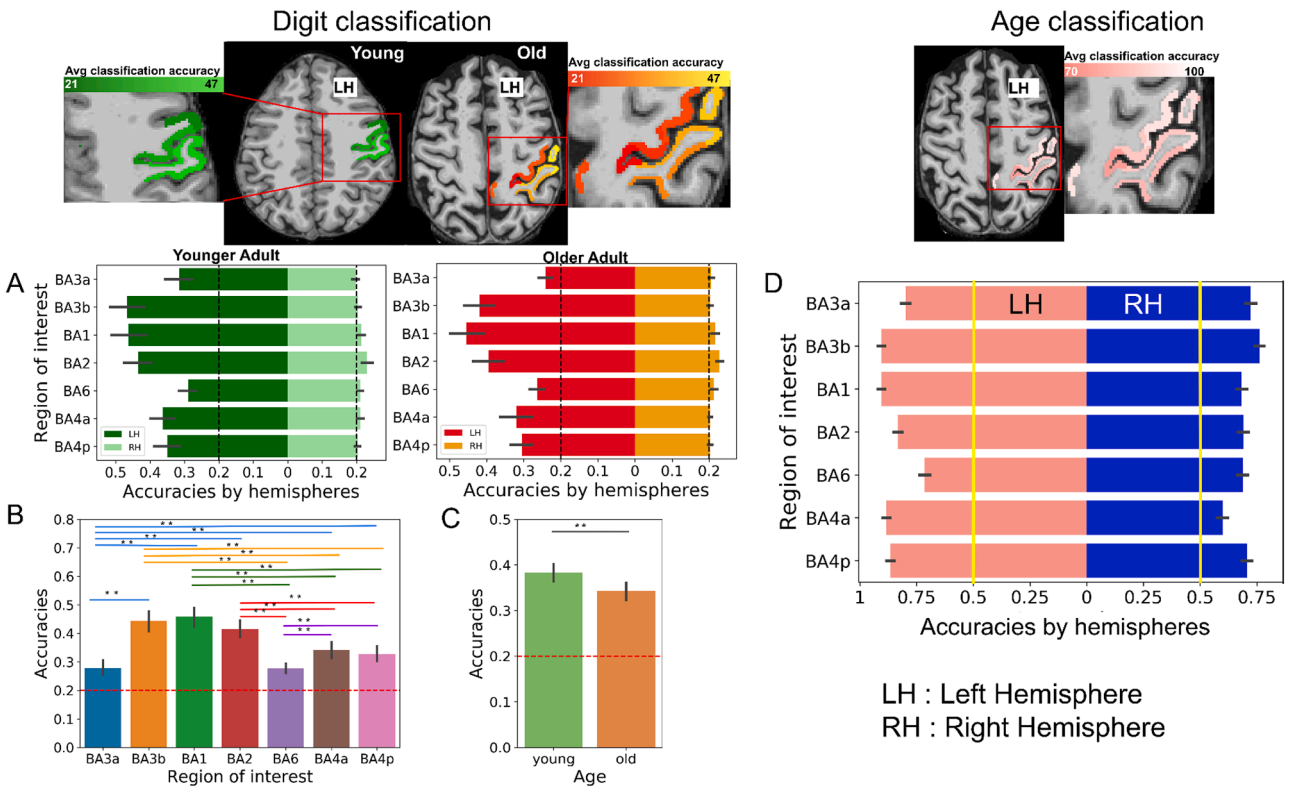

Fig. 3. Sensory Finger Decoding in Different BAs in Younger and Older Adults. A: Bar plots show ROI-based decoding accuracies for the left and right hemispheres obtained by responses to digit stimulation in younger and older adults. Average accuracies are mapped over the brain at the top row (younger (green) and older (red) adults). The black dotted line indicates chance level for finger classification (5 classes, chance accuracy (i.e. Ac_{chance}) = 0.2)). **B:** Significant main effect of ROI in digit-discriminating decoding accuracies. Asterisks represent significant differences at the $p<0.05$ level, and double asterisks represent significant differences at the $p<0.005$. Colours indicate the different regions of interest. **C:** Significant main effect of age group in digit decoding accuracies, (younger (green) and older (orange) adults). Double asterisks represent significant differences at the $p<0.005$ level. **D:** Comparison between age group decoding accuracy between right (ipsilateral) and left (contralateral) hemispheres using rSRM. Note that tactile stimulation was provided to the fingers of the right hand. Error bars represent the standard error over the mean scores obtained using SVM. The yellow line indicates chance level for age classification (2 classes, Ac_{chance} = 0.5). (For interpretation of the references to color in this figure legend, the reader is referred to the web version of this article.)

LAYNII2 (i.e. Version 2.0 of Laynii) (command: LN2_COLUMNS) (Huber et al., 2021). This command runs an algorithm that generates approximately equal volume columns in the T1-MRI image by using the middle gray matter segment as the input, which is generated by LN2_LAYERS (i.e. the cortical columns were defined based on gray matter anatomy after performing structure to functional registration). Then, the means of all thresholded voxels within a cortical column were used to compute a matrix: columns by time-series (see Fig. 5C). To summarize, we first used cortical anatomy to define different numbers of cortical columns. Later in the analyses, the mean of the voxel values that were present in a given column were used for data modeling. For given different numbers of columns were used as an input, the number of voxels that composed one column also varied between the analyses. This was done for both cyclic runs and across BA1 and BA3b for all participants. Then, this matrix was used to train the rSRM using cross-validation, as described in the previous section (see Section 2.4.1.2). Linear SVM-based leave-one-subject-out decoding analyses were performed separately for (10, 20,..., 400) number of columns to determine the number of columnar divisions that best captures the functional features. In this way, we modeled the functional activation patterns to find the optimal number of columns, which were initially generated based on anatomy of the cortex. We plotted the number of columns against the respective average decoding accuracies and standard deviation, we then did a Gaussian curve fitting to the accuracies and detected the individual peak to identify the average individual columnar size with best accuracy.

2.5. Statistical analyses

A two-way ANOVA with the factors age (younger, older) and ROIs (BA1, BA2, BA3a, BA3b, BA4a, BA4p, and BA6) was calculated on the digit classification accuracies to test the influence of both factors, and the interaction between both factors, on the digit classification scores in the ROI specific analyses in the left hemisphere. For significant main effects or interactions, post hoc independent sample t-tests were computed. The statistical tests were performed in Python using the 'statsmodels' package. An alpha level of $p<0.05$ was used to test for the significant main effects and interactions, and for significant post hoc test results. We also performed a permutation test to evaluate the digit and age decoding models. For this, we permuted the target (i.e. age labels) to generate randomized data and computed the 'p' (p-value) against the null hypothesis that the shared-space features and age labels are independent. We also computed t-test for the neighbouring Euclidean distances for the random-design analysis in the Supplementary Material S1, 2, to check for the significance increase of the distances along adjacent neighbours.

3. Results

3.1. Finger-specific sensory decoding in different BAs

Different brain areas respond differently to somatosensory stimulation, in particular with respect to signal specificity. In this section, we use rSRM to describe the hierarchical encoding of somatosensory stimuli

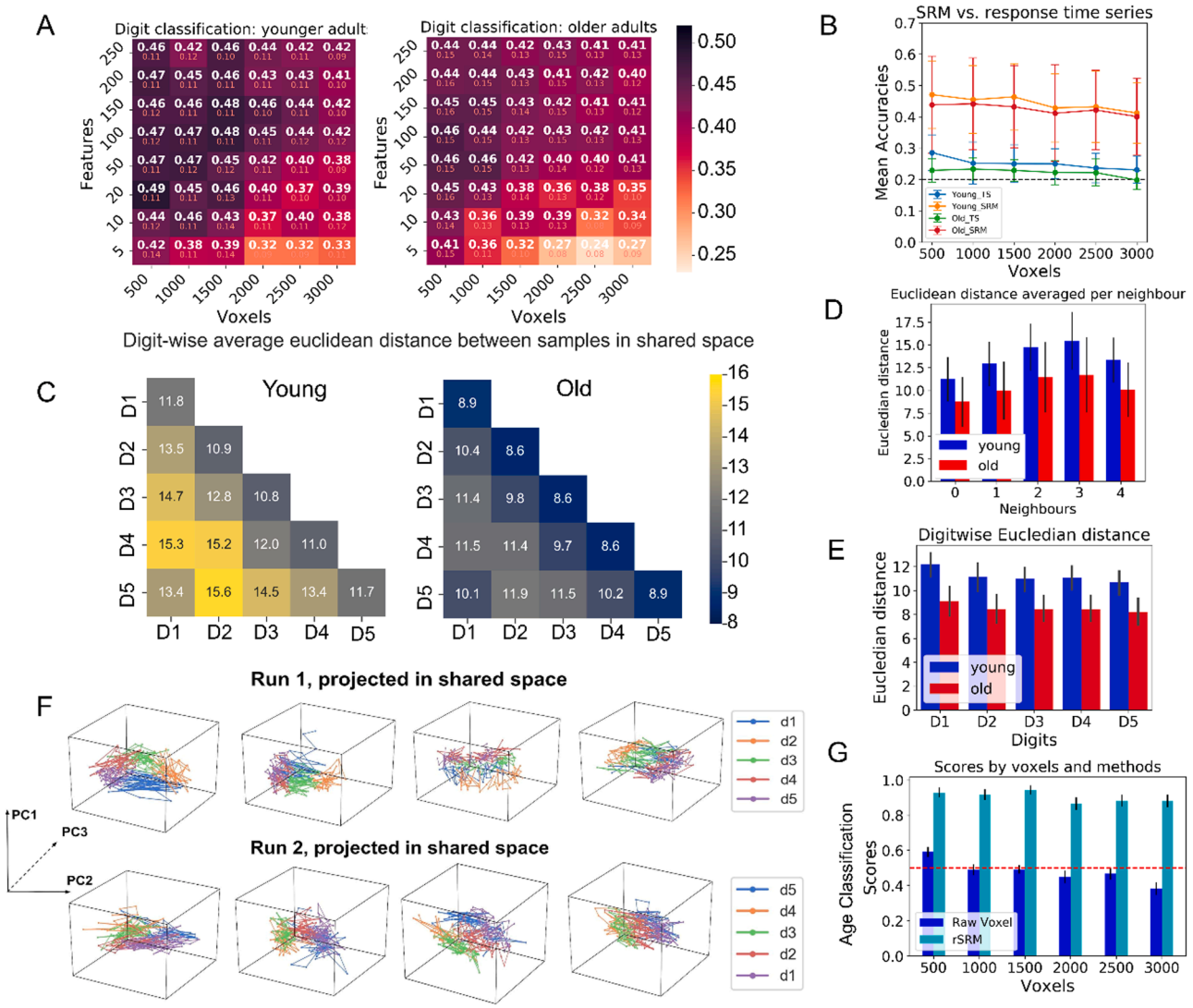

Fig. 4. Age-related rSRM Digit Classification A: Heatmaps show mean accuracies and standard deviations of different feature numbers and numbers of voxels. Accuracies were obtained by leave-one-subject-out cross-validation using SVM with a linear kernel. **B:** Line plots show the unaggregated time-series-based (*green* for younger and *blue* for older adults) and rSRM-based (*orange* for younger and *red* for older adults) digit decoding accuracies (with k = 200); error bars show the standard deviation. **C:** Average Euclidean distances between samples in shared space generated using rSRM with K = 5 features for younger and older adults. The low values in the diagonal and the higher values in the off-diagonal show that similar digit responses are closer to each other and increases gradually along the first, second, third, and decreases again for fourth neighbour. **D:** Bar graphs show average Euclidean distances as in **C** but ordered along the dimension of neighbour (first, second, third, fourth neighbour, note that there are more first then second neighbours, more second than third neighbours, and more third than fourth neighbours) and with a direct comparison between younger (*blue*) and older (*red*) adults. Error bars indicate standard deviations. **E:** Bar graphs show average Euclidean distances for younger (*blue*) and older (*red*) adults digit-wise. Error bars indicate standard errors of the mean. **F:** Top three principal components obtained by PCA of run D1 -> D5 and run D5 -> D1 projected into shared space. The three axes represent the principal components of the shared response in the 3D representational space. Digits are arranged circularly in 3D space for 4 different example subjects. NOTE: PCA was only performed for visualization purposes this is not part of any of the analyses. **G:** Bar graphs show mean age group decoding accuracies of the fMRI time series unaggregated (*blue*), and rSRM based approach (*cyan*). Accuracy scores were obtained by using linear SVM. The error bars represent the standard error of mean. (For interpretation of the references to color in this figure legend, the reader is referred to the web version of this article.)

in higher- and lower-order somatosensory and motor cortices of the hemisphere contralateral to the stimulation (right hand stimulation, left hemisphere). To this aim, we compared sensory decoding accuracies across different Brodmann areas (BA1, BA2, BA3a, BA3b, BA4a, BA4p, and BA6) in the left hemisphere and the areas in the right hemisphere as control. In both age groups, BA1 and BA3b revealed the highest mean decoding accuracies (BA1: accuracy younger: 0.46 ± 0.12, accuracy older: 0.45 ± 0.10, BA3b: accuracy younger: 0.47 ± 0.12, accuracy older: 0.42 ± 0.10), followed by BA2 (accuracy younger: 0.43 ± 0.09, accuracy older: 0.39 ± 0.10), BA4a (accuracy younger: 0.36 ± 0.08, accuracy older: 0.32 ± 0.10) and BA4p (accuracy younger: 0.35 ± 0.09, accuracy older: 0.31 ± 0.07). Lowest accuracies were revealed for BA6 (accuracy younger: 0.29 ± 0.06, accuracy older: 0.26 ± 0.06) and BA3a (accuracy younger: 0.32 ± 0.09, accuracy older: 0.24 ± 0.04) (see Fig. 3). The right hemisphere showed the mean decoding accuracy of around chance (i.e. ~0.20) across different regions for younger and older adults. Given that BA3b and BA1 are known to contain the most precise topographic finger maps in younger adults (Pfannmöller et al., 2016), our methodological approach supports this finding and additionally reports this for the first time for older adults.

We additionally calculated if within this given processing hierarchy, age-differences would be apparent. A two-way ANOVA with the factors age (younger, older) and BA (BA 1, 2, 3a, 3b, 4a, 4p and 6) revealed a main effect of age ($F(1) = 14.13$, $p = 2.12e\text{-}04$) and a main effect of BA

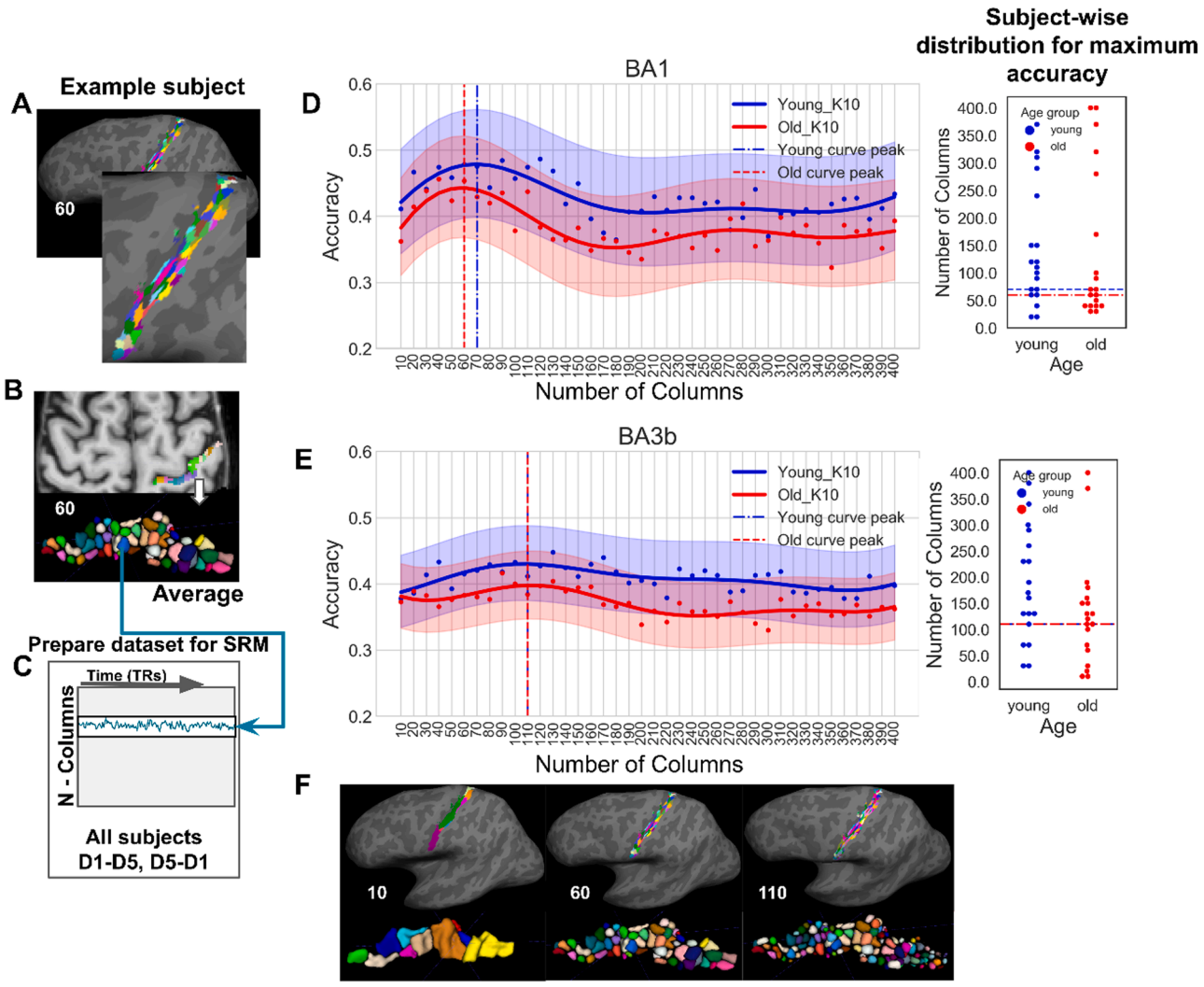

Fig. 5. Column-Based SRM (C-SRM) A: An example subject's 60 columns projected to the surface in BA3b **B, C:** The anatomical data show 60 numbers of columns in BA3b in volume space, and a schematic overview of how the shared response space is generated for N different numbers of columns. **C:** Dataset matrix represents averaged time-response of voxels present in each column for one of the two run types (D1 to D5, D5 to D1). **D-E:** Means (*solid lines*) and standard deviations (*semi-transparent spread*) of digit classification scores over a range of columns and different age groups; 10 features were used to train the rSRM; the plot is a smoothed curve obtained by Gaussian smoothing for a window-size of 6. **D:** Mean and standard deviation of digit decoding scores in ROI BA1 shown for different numbers of columns; the different colours indicate the age groups (younger subjects: *blue*, older subjects: *red*); *vertical dashed lines* indicate curve maxima); a subject-wise distribution with the number of columns at which the maximum accuracy was achieved is shown in the adjacent plots (*right*). **E:** same as (**D**) but for the ROI BA3b. **F:** Visualization of different columns on the surface and in the volume space of BA3b. (For interpretation of the references to color in this figure legend, the reader is referred to the web version of this article.)

(F(6) = 27.78, p = 2.17e-25) in digit classification accuracies, but no significant interaction effect between BA and age (F(6) = 0.49, p = 0.815) in the left hemisphere. The main effect of age was due to older adults showing generally worse decoding accuracy compared to younger adults across different BAs (average accuracy, younger: 0.38 ∓ 0.11; older: 0.34 ∓ 0.10).

The main effect of BA was due to (i) significantly lower accuracy of BA3a compared to BA3b (BA3a: 0.28 ± 0.08, BA3b: 0.44 ± 0.11, t(74) = 7.52, p = 1.02e-10), BA1 (BA1: 0.46 ± 0.11, t(74) = 8.09, p = 8.61e-12), BA2 (BA2: 0.41 ± 0.09, t(74) = 6.89, p = 1.59e-9), BA4a (BA4a: 0.34 ± 0.09, t(74) = 3.23, p = 0.002), and BA4p (BA4p: 0.33 ± 0.08, t (74) = 2.66, p = 9.49e-03); (ii) significantly higher accuracy of BA3b compared to BA4a (t(74) = 4.43, p = 3.16e-05), BA4p (t(74) = 5.18, p = 1.87e-06), and BA6 (BA6: 0.28 ± 0.05, t(74) = 8.44, p = 1.93e-12); (iii) significantly higher accuracy of BA2 compared to BA4a (t(74) = 3.51, p = 7.68e-04), BA6 (t(74) = 7.94, p = 1.66e-11), BA4p (t(74) = 4.31, p = 5.02e-05).

Taken together, these data show that, whereas the processing hierarchy is preserved across age groups, older adults show generally worse decoding accuracies across the tested BAs.

3.2. *Fine-grained SI topography in different age groups*

Next, we used rSRM to compute across-run digit and age classification to more specifically target the question of whether rSRM can be used to describe the above reported age-related changes in the topographic SI architecture in more detail. Note that in the analyses reported above, we show generally lower decoding accuracies as a main effect of age across all BAs, whereas here, we explore the *features* that drive these differences in more detail. We first tested the digit decoding capability of the model. By doing so, we investigated if the number of statistically significant voxels included in the analyses has an influence on the overall decoding accuracy of the digits. This was tested for younger and older adults separately. We found that a higher number of voxels resulted in a higher dimensional feature space capturing the shared response and explaining the shared variance. For example, in younger

adults, to obtain an average accuracy of 0.42 ± 0.14, 500 voxels needed 5 number of features in the shared space, whereas 3000 voxels needed 100 number of features in the shared space to obtain the similar decoding accuracy (see Fig. 4A). This was similar for younger and older adults (in spite of the above mentioned lower decoding accuracies in older compared to younger adults). For further analyses, the optimal number of voxels for the ROI-based analysis was chosen (i.e., n_{Voxels} = 500), with the lower number of features (k =10) explaining most of the shared variance across subjects.

Using these parameters, we then tested the performance of the rSRM against the unaggregated functional time series based tactile stimulus decoding, and age-group decoding using leave-one-subject-out cross-validation and SVM classification. Here, we first compared the tactile stimulus decoding accuracy in younger and older adults when separately modeled in a shared space using time-series-based classification. We observed that the rSRM-based stimulus decoding outperforms the unaggregated time-series-based decoding (e.g. average accuracy scores at 500 voxels selected for younger rSRM (k = 200) : 0.47 ± 0.11; younger unaggregated time-series: 0.29 ± 0.06, older rSRM: 0.44 ± 0.16; older unaggregated time-series: 0.23 ± 0.04), hence confirming that rSRM can successfully capture the shared tactile information across subject groups (see Fig. 4B). Even in the case of age-based decoding analysis, rSRM-based decoding performs better than the unaggregated time-series-based decoding (see Fig. 4G, blue bar) with scores around chance level of 0.5, whereas the overall average accuracy achieved using rSRM is 0.90 ± 0.05 (see Fig.e 4G). The bar plot (cyan bar) represents the average age decoding accuracy of 0.90 ± 0.05 when separate models were trained in order to learn their respective shared feature space. The accuracies obtained were above chance level (i.e. above 0.5). When separate models are used to learn the shared feature space, the mean decoding accuracy shows that group-specific differences exist, and separate models learn the features shared within a group. We repeated the same analysis with K = 50, in different BAs across both hemispheres and found that the overall age group classification accuracies in the left hemisphere was higher (mean ± SD; 0.84 ± 0.26) and lower in the right hemisphere (mean ± SD;0.69 ± 0.31) this achieved accuracy could be an effect of increased bilateral activation in older adults (see Fig. 3D).

We also performed a permutation test to evaluate the significance of the accuracies obtained by two-fold cross-validation. The dependency between the unaggregated time-series based feature and age labels was low (with p = 0.068) whereas the relationship between the features and age-group labels when the separate shared spaces were used for both the age-groups was high (with p = 0.001). This indicates that the age classification accuracies were not obtained by chance.

Given this approach, we then computed digit classification and Euclidean distances to define age-specific changes that may target only specific fingers, or only specific neighbours (see Fig. 4C). Euclidean distance was measured in the response-driven shared feature space with k = 5 as the number of feature dimensions for training the rSRM; we here assumed that each dimension represents one digit. For both younger and older adults, the diagonal values are smaller than the off-diagonal values, which suggests, as expected, that the sample points corresponding to the same digit are more similar than the neighbouring digits in the shared feature space. The first (mean ± SD; younger: 11.24 ± 2.43, older: 8.73 ± 2.72), second (younger: 12.94 ± 2.45, older: 9.99 ± 3.18) and third neighbours (younger: 14.77 ± 2.56, older: 11.44 ± 3.88) show subsequent increase in the averaged Euclidean distances, whereas this reduces for the fourth neighbour (younger: 13.35 ± 2.44, older: 10.07 ± 2.99) in case of both younger and older subjects. The drop in distances could indeed be attributed to the fact that D5 and D1 were stimulated directly after one another. This effect was further investigated in an additional analyses conducted on the random-design data in the Supplementary Material S1, 2. This analysis revealed that the Euclidean distance does not significantly increase further after neighbour 3 (Younger subjects, t(18) = 1.66, p = 0.11, with neighbour 3: 5.93, neighbour 4: 6.0; Older subjects t(18) = 0.86, p = 0.40, with neighbour 3: 4.01, neighbour 4: 4.03, see 2, Figure S2, Supplementary Material S1,). In addition, an overall difference in the similarity measure using the Euclidean distance can be observed across age groups with the average Euclidean distance being higher in younger adults as compared to older adults (see Fig. 4C, D).

Taken together, the above described results show that i) digit decoding is generally lower for older compared to younger adults, ii) in the shared space, the sample points representing different digits were observed to be arranged in closer proximity to itself (this pattern was consistent for both younger and older adults, see Fig. 4D), iii) the Euclidean distance measure for older adults is lower compared to younger adults across different digits and neighbours, and iv) the ipsilateral hemisphere shows around chance digit decoding accuracy and lower age decoding accuracy as compared to the contralateral hemisphere. (see Fig. 3)

3.3. Columnar-Shared Response Modeling (C-SRM)

Finally, we used the above outlined methodology to investigate columnar units in SI. As outlined in the introduction, sensory and motor cortices can be divided into columnar units, which helps to detect fine-grained topographic maps with high precision (Yacoub et al., 2008; Yang et al., 2019; Huber et al., 2020). We here aim to identify the number of columns required to effectively decode the SI generated responses, i.e., the topographic map of the fingers triggered by passive touch in younger and older adults. Because 16 pin combinations were used to stimulate each finger, the data could potentially identify columnar units that are smaller than one finger representation. We divided the cortex into different numbers of columns, and plotted the results against the respective decoding accuracies, we then did a Gaussian curve fitting to the accuracies and detected the individual peak to identify the columnar size with best accuracy.

Across different columnar divisions, mean accuracies were higher in BA1 compared to BA3b in both younger and older adults (see Fig. 5D,E). Interestingly, we observe that the average column size that best predicts the digits were different for younger and older adults in BA1 but not in BA3b. Please note that columnar size here does not relate to anatomical cortical columns as defined based on changes in myelination, for example, Doehler et al. (2023), Kuehn et al. (2017), but represents an anatomical unit that is defined based on T1-based cortical modeling using LAYNII, which does not take into account different T1 values in different cortical areas. The question how these units relate to structural units that have different myeloarchitecture in S1 is not answered here. In BA1, the finger map of younger adults was best represented by more columns compared to older adults (BA1: younger: 70 (average columnar size: 44.26 ± 5.06 mm^3), older: 60 (average columnar size: 45.47 ± 5.55 mm^3); whereas it was the same columnar number in BA3b (both 110 for younger (average columnar size: 28.94 ± 3.51 mm^3) and older (average columnar size: 24.49 ± 2.40 mm^3) adults. Note that for a columnar size of 27 mm^3, the dimensions are 3×3×3 mm, just to give an example.

Taken together, we here combine rSRM with columnar analyses (a method that we introduce as C-SRM) to offer a statistical approach to calculate the number of columns that best represents finger differentiation in different BAs of SI. We show that in BA3b, 110 columns best represent the smallest unit of finger differentiation in younger and older adults, whereas the columnar number is higher for younger adults in BA1, indicating smaller computational units in younger adults. Please note that the different columnar sizes in younger and older adults could be driven by both higher precision and reduced noise (see more details in Discussion section).

4. Discussion

Here, we used robust shared response modeling (rSRM) and introduced columnar-SRM (C-SRM) to describe architectural features of somatosensory finger representations in younger and older adults. We

show that the somatosensory processing hierarchy is not significantly different between younger and older adults, as denoted by highest digit-classification accuracies in BA1 and BA3b, followed by BA2, BA4a, BA4p, BA6, and finally BA3a. We also show that digit-classification accuracy was lower for older adults as compared to younger adults across these different BAs, and around chance in the hemisphere ipsilateral to the stimulation. Please note that these group differences are likely not driven by differences in tactile sensitivity as the stimulation intensity was adjusted to the individual tactile detection threshold in each individual. We further show that the average Euclidean distance across sample points in the feature space is lower for older adults as compared to younger adults across digits and finger neighbours. We also introduce a new analysis approach, C-SRM, that we use to detect the optimal columnar size required to efficiently decode finger representations in SI in different age groups. The results show that for finger decoding, a lower number of columnar units (hence a larger columnar size) is optimal in older adults as compared to younger adults in BA1, which indicates larger computational units in older adults' sensory SI processing. Together, our results allow a better understanding of basic functional features of somatosensory processing and their change with increasing age. The methods used and introduced here also allow modeling shared and distinct features of sensory maps using voxels or columns as input units that allows studying fine-grained functional units and their group-dependent differences in greater detail.

We performed a region-of-interest (ROI) based analysis to determine the hierarchical representations of digits across different somatosensory and motor areas in the left and the right hemispheres. In previous studies on hierarchical processing of somatosensory information, it has been reported that a Iarge portion of BA2 neurons receive tactile inputs from areas BA3b and BA1, and that tactile neurons in BA2 therefore have more complex and larger population receptive fields and response properties than those in areas BA3b and BA1 (Gardner, 1988). Hierarchical processing is here defined as the level of precision with which touch to a specific finger causes a distinct representation in the cortex. Lower-hierarchical processing therefore assumes higher decoding accuracies (i.e., more precise representation of each finger), whereas higher-hierarchical processing assumes lower decoding accuracies (i.e., less precise representation of each finger, and potentially greater influence of high-level processing). This previous finding was confirmed by our analyses, where both younger and older adults showed highest finger decoding accuracies in BA3b and BA1, followed by BA2 in the hemisphere contralateral to the stimulation (i.e., left hemisphere).

However, prior research has rarely investigated somatosensory finger representations in motor areas and BA3a, and has also not yet described potential age-dependent differences in the processing hierarchy. Our data reveal that finger-specific representation of tactile input is better (as revealed by decoding accuracy in the left hemisphere) in motor cortical areas BA4a, BA4p, and BA6 compared to somatosensory BA3a both in younger and older adults. Our data also indicate that there is more finger-specific information represented in anterior compared to posterior primary motor cortex, and compared to premotor cortex both in younger and older adults. In addition, our analyses reveal that whereas decoding accuracy is generally lower in older compared to younger adults, there is no interaction between age and BA. Therefore, age effects were homogeneous across the different areas that process somatosensory information. Our data therefore indicate that even though older adults represent each finger less distinct, the precision hierarchy (i.e., BA1 & BA3b > BA2 > BA4a > BA4p > BA6 > BA3a) is preserved across age groups, and there is no area where somatosensory deterioration clearly precedes in healthy aging. Another possibility is that these accuracies can also indicate less noise and the presence of information (Gardumi et al., 2016).

We used rSRM to detect digit- and age-specific differences in SI and compared it with an unaggregated time-series based decoding method. We found that the rSRM-based method performs better than the unaggregated time-series based method (quantified on the basis of classification accuracy), and that rSRM successfully captures the digit-based and age group-based variances. The reasons for this difference may be age-related sensory processing differences, e.g. the decline in touch sensitivity at older age, and that a separate model may learn this group-specific difference more accurately. We also show that when separate models for younger and older adults are used to learn the shared feature space across different brain regions, the mean age group decoding accuracy is higher in the hemisphere contralateral to the stimulation, as compared to the hemisphere ipsilateral to the stimulation. This indicates that features of the functional architecture that are specific to tactile processing are driving the age-related differences, rather than differences that are not specific to the tactile stimulation. However, we observed that even though the decoding accuracy in the ipsilateral hemisphere is lower, it is still significant above chance some regions. One possible reason is the increased bilateral integration of functional activations in older adults compared to younger adults. This phenomenon is commonly referred to as the "hemispheric asymmetry reduction in older adults" (HAROLD) model, as initially introduced by Cabeza (2002). In subsequent studies, this effect has also been observed in the motor cortex and has been discussed as a potential indicator of compensation (Knights et al., 2021). Alternatively, given somatosensory information is known to integrate across hemispheres, it is also possible that the same features that allowed successful decoding in the contralateral hemisphere also allowed successful decoding in the ipsilateral hemisphere. Finally, also functional features other than the two listed above may account for successful age group decoding in the ipsilateral hemisphere.

We also investigated the shared feature space in more detail using the Euclidean distance measure and found that the samples representing the individual digits were arranged close to each other. We performed principal component analysis (PCA) over the projected shared space and observed that the sample points corresponding to the specific digits in one given run were clustered together in the 3D component space, and almost formed a ring-like structure reflecting the nature of digit stimulation (note that stimulation order was "D1 to D5" or "D5 to D1"). This is a relevant observation as it indicates that rSRM captures the stimulus-specific brain activity that is shared across the subjects rather than being affected by the spatial mismatch of functional topographies. In addition, even though the cyclic design has an influence on the Eucledian distance measure resulting in lower 4th neighbour distances (i.e. between D1 and D5), the model effectively captures the digit-specific features in the shared space. To support this argument, we did an additional analysis with the random-design data where our model was able to capture and decode digit-specific features for younger and older adults. The details of this additional analysis can be found in the Supplementary Material S1 and Supplementary Material S2. It is worth noting that the Eucledian distance was estimated in the reduced dimensional feature space of the test data, and should therefore have no topographical relevance.

In our study, we utilized random-design data as the localizer for ROI definition and analysis, as described in the work by Liu et al. (2021). Random-design allowed for individualized localization of each digit, while phase-encoded mapping, as discussed in the study by Besle et al. (2013), provided higher sensitivity to detect subtle map differences. The phase-encoded design enabled differentiation between neighboring areas with opposite phase signs, ensuring accurate mapping of cortical organization (Sereno et al., 1995). Conversely, random-design was preferred for unbiased localization and computation of representational overlap. Furthermore, Kassraian et al. (2022) demonstrated that expected vibrotactile stimulation of specific digits yielded higher decoding accuracy compared to non-expected stimulation.

Finally, we here introduce a novel approach for detecting the optimal number of equi-volume columns in which the cortex can be effectively divided in order to describe topographic maps. Note that this method computes decoding analyses on mean voxel activations that were ordered along columnar units before performing the analyses. One

precondition for the model is therefore the assumption that meaningful information is present within one columnar unit and across cortical depths (Huber et al., 2017). It is also of note that this model disregards the dimension of the layer, therefore, it is only recommended if the focus is on organizational features that are organized along the cortical surface. We named the method C-SRM to highlight the combination between columnar modeling (C) and shared response modeling (SRM). C-SRM may be a relevant new method given prior studies used different columnar sizes to describe topographic maps without providing a reason or statistical approach to justify these numbers. For BA3b, we show that the same number of cortical columns provides highest decoding accuracies for both younger and older adults, even though the analyses were performed separately for each group. This result of 110 equi-volume columns that best represent the number of units that describe topographic finger maps in BA3b is therefore robust and was replicated within both age groups. Given this analysis was done in the a priori defined finger map area, this corresponds on average to 22 columns per digit, which is close to the 16 pin combinations that were used for stimulating each digit. If confirmed by future research, this would indicate that columnar mapping can be used to detect the computationally smallest unit in BA3b.

Interestingly, we also found that the maximum decoding accuracy for older adults was achieved at a lower number of columns for BA1 compared to younger adults. Whereas for younger adults, 70 columns in BA1 best distinguished fingers, for older adults, this was the case for 60 columns in BA1. If we consider the above outlined argument that one column may represent the computationally smallest unit, this aligns with the recent finding that the somatosensory receptive field size for older adults are larger as compared to the younger adults (Liu et al., 2021). One biological mechanism that one could therefore hypothesize to underlie these results is that the increased population receptive field size in older compared to younger humans leads to an enlargement of the columnar units that characterize the system. In prior research, reduced intracortical inhibition has been hypothesized to be one mechanism underlying larger sensorimotor representations in older age (Pleger et al., 2016; Ruitenberg et al., 2019). Another possibility would be altered top-down control of sensory processing in older compared to younger adults, differences in sensory attention, or differences in the structural layer architecture.

Also the visual cortex contains a hierarchy of visual areas. The earliest cortical area (V1) contains neurons which respond to colour, form and motion, and the second visual area (V2) contains a stripe-based anatomical organization, as has been shown in non-human primates (Lund et al., 2003). Neurons in these stripes have been proposed to serve distinct functional roles, e.g. the processing of colour, form and motion. These stripes represent an intermediate stage in the visual hierarchy and serve a key role in the increasing functional specialization of visual areas. In the visual cortex, there are also distinct microstructural features that characterize cortical columns (Erwin et al., 1995). One study investigated ocular dominance columns (ODC) (Chaimow et al., 2018b), which is a structure that can be spotted in ex vivo cytochrome oxidase stainings, and that has a distinct functional and connectivity architecture. Neighboring areas in the visual cortex encode different features (in this case different orientations), resulting in a distinct structure. In our case, however, neighboring areas in the finger encode neighboring skin locations, they are therefore most likely structurally less distinct from one another compared to ODCs. Whether or not our described columnar model also has a structural component in SI and is, for example, accompanied by alterations in neuronal or myelin architectures, remains to be investigated (Doehler et al., 2023).

In a study performed by Chaimow et al. (2018a), the authors provide valuable insights into optimizing fMRI parameters to detect and decode response patterns of cortical columns using high-resolution fMRI data at 7T. They specifically investigate the influence of factors such as the spatial scale of columnar patterns, point spread of fMRI response, voxel size, and signal-to-noise ratio (SNR). Of particular relevance to our study, the authors conducted experiments with various voxel sizes to determine the voxel resolution that best decodes multiclass data across columns. Through their investigations, they identified an optimal voxel width of approximately 1 mm, which maximized decoding accuracy. They also found that the width of the point spread function had a significant impact on decoding and reconstruction measures for Gradient and Spin Echo at 7T, while response amplitudes played a minor role. In our work, we utilized a 1 mm voxel size, which aligns with the suggestions made in the aforementioned paper. However, it is important to note that we did not simulate different voxel sizes to identify the optimal one, as the size of functional units in SI is not yet fully understood. Instead, the voxel size was fixed and we varied the columnar sizes to determine the optimal decoding accuracy. The choice of the voxel size in our study was motivated by obtaining an optimal SNR considering the number of trials per block. We therefore acknowledge that choosing a different voxel size may also influence the columnar modeling results. Future studies should therefore apply the present approach using different voxel sizes to optimize this parameter for SI.

Taken together, different rSRM-based methods were used here to investigate group differences in ultra-high-resolution data. In combination with columnar mapping, our study introduces a novel approach to map fine-grained features of sensory space that can be used to identify the smallest computational unit along the cortical surface, such as responses to pin stimulations. Even though future research has to clarify some of the open aspects mentioned above, this analysis method may inspire future research to detect functionally and anatomically relevant units in ultra-high resolution data, and to compute the data in a shared space.

5. Conclusion

Here, we aggregate UHF-fMRI group data using rSRM, and report the model to be successful in capturing digit-specific tactile information in the sensorimotor cortex. We also introduced a novel method, C-SRM, for identifying the optimal number of equi-volume columnar units to achieve the highest somatosensory decoding accuracy that may be a promising approach to combine structural and functional high-precision analyses in the future. rSRM also successfully identified age-specific shared variances across age groups (younger and older adults), which makes it a potentially suitable tool for intersubject alignment. The analyses presented here may in the future be used in UHF-fMRI studies to capture the variability across groups and brain regions, and to detect specific responses to small processing units. C-SRM can also be applied to other sensory regions of the brain and reveal information about the optimal number of columnar units.

Data and code availability statement

The data were recorded at a whole-body 7 Tesla Siemens MRI scanner in Magdeburg.

(https://osf.io/2uwze/?view_only=e29c70a83d574b42870e2aed01d07b1e)

The codes for analysis are available at (https://github.com/avinashkalyani/somato_align_age_WB)

Data availability

https://osf.io/2uwze/?view_only=e29c70a83d574b42870e2aed01d07b1e.

Code availability

https://github.com/avinashkalyani/somato_align_age_WB.

CRediT authorship contribution statement

Avinash Kalyani: Conceptualization, Investigation, Formal analysis, Methodology, Writing – original draft. **Oliver Contier:** Conceptualization, Methodology, Writing – review & editing. **Lisa Klemm:** Methodology, Writing – review & editing. **Elena Azañon:** Methodology, Writing – review & editing. **Stefanie Schreiber:** Writing – review & editing. **Oliver Speck:** Conceptualization, Methodology, Writing – review & editing. **Christoph Reichert:** Supervision, Conceptualization, Methodology, Writing – review & editing. **Esther Kuehn:** Supervision, Investigation, Conceptualization, Methodology, Writing – review & editing.

Declaration of Competing Interest

The authors declare that they have no known competing financial interests or personal relationships that could have appeared to influence the work reported in this paper.

Data availability

The data and code information has been shared in the manuscript

Acknowledgments

This work was funded by the Deutsche Forschungsgemeinschaft (DFG, German Research Foundation): Project-ID 425899996, SFB 1436 and KU 3711/2-1, Project-ID: 423633679. Avinash Kalyani was funded by the Center for Behavioral Brain Sciences Magdeburg - CBBS gefördert durch EFRE, Förderkennzeichen: ZS/2016/04/78113.

Supplementary materials

Supplementary material associated with this article can be found, in the online version, at doi:10.1016/j.neuroimage.2023.120430.

References

Al-Wasity, S, Vogt, S, Vuckovic, A, Pollick, FE., 2020. Hyperalignment of motor cortical areas based on motor imagery during action observation. Sci. Rep. 10, 5362. https://doi.org/10.1038/s41598-020-62071-2.

Besle, J, Sánchez-Panchuelo, R-M, Bowtell, R, Francis, S, Schluppeck, D., 2013. Single-subject fMRI mapping at 7 T of the representation of fingertips in S1: a comparison of event-related and phase-encoding designs. J. Neurophysiol. 109, 2293–2305. https://doi.org/10.1152/jn.00499.2012.

Brett, M, Johnsrude, IS, Owen, AM., 2002. The problem of functional localization in the human brain. Nat. Rev. Neurosci. 3, 243–249. https://doi.org/10.1038/nrn756.

Cabeza, R., 2002. Hemispheric asymmetry reduction in older adults: the HAROLD model. Psychol. Aging 17, 85–100. https://doi.org/10.1037/0882-7974.17.1.85.

Cassady, K, Ruitenberg, MFL, Reuter-Lorenz, PA, Tommerdahl, M, Seidler, RD., 2020. Neural dedifferentiation across the lifespan in the motor and somatosensory systems. Cereb. Cortex 30, 3704–3716. https://doi.org/10.1093/cercor/bhz336.

Chaimow, D, Uğurbil, K, Shmuel, A., 2018a. Optimization of functional MRI for detection, decoding and high-resolution imaging of the response patterns of cortical columns. Neuroimage 164, 67–99. https://doi.org/10.1016/j.neuroimage.2017.04.011.

Chaimow, D, Yacoub, E, Uğurbil, K, Shmuel, A., 2018b. Spatial specificity of the functional MRI blood oxygenation response relative to neuronal activity. Neuroimage 164, 32–47. https://doi.org/10.1016/j.neuroimage.2017.08.077.

(Cameron) Chen, P-H, Chen, J, Yeshurun, Y, Hasson, U, Haxby, J, Ramadge, PJ, 2015. A Reduced-Dimension fMRI Shared Response ModelAdvances in Neural Information Processing Systems. Curran Associates, Inc.

Cohen, JD, Daw, N, Engelhardt, B, Hasson, U, Li, K, Niv, Y, Norman, KA, Pillow, J, Ramadge, PJ, Turk-Browne, NB, Willke, TL., 2017. Computational approaches to fMRI analysis. Nat. Neurosci. 20, 304–313. https://doi.org/10.1038/nn.4499.

Dervin, J., 1990. Co-planar stereotaxic atlas of the human brain 3-dimensional proportional system: an approach to cerebral imaging 1988J. Talairich and P. Tournoux Mark Rayport Georg Thieme Verlag. Stuttgart, New York 3 13 711 701 1 Price DM 268. pp. 122. Illustrations 130. J. Laryngol. Otology 104, 72.

Doehler, J, Northall, A, Liu, P, Fracasso, A, Chrysidou, A, Speck, O, Lohmann, G, Wolbers, T, Kuehn, E., 2023. The 3D structural architecture of the human hand area is nontopographic. J. Neurosci. 43, 3456–3476. https://doi.org/10.1523/JNEUROSCI.1692-22.2023.

Erwin, E, Obermayer, K, Schulten, K., 1995. Models of orientation and ocular dominance columns in the visual cortex: a critical comparison. Neural Comput. 7, 425–468.

Feilong, M, Guntupalli, JS, Haxby, JV, 2021. The neural basis of intelligence in fine-grained cortical topographies. eLife 10, e64058. https://doi.org/10.7554/eLife.64058.

Feilong, M, Nastase, SA, Guntupalli, JS, Haxby, JV., 2018. Reliable individual differences in fine-grained cortical functional architecture. NeuroImage 183, 375–386. https://doi.org/10.1016/j.neuroimage.2018.08.029.

Fischl, B, Sereno, MI, Tootell, RB, Dale, AM., 1999. High-resolution intersubject averaging and a coordinate system for the cortical surface. Hum. Brain Mapp. 8, 272–284.

Gardner, EP., 1988. Somatosensory cortical mechanisms of feature detection in tactile and kinesthetic discrimination. Can. J. Physiol. Pharmacol. 66, 439–454.

Gardumi, A, Ivanov, D, Hausfeld, L, Valente, G, Formisano, E, Uludağ, K., 2016. The effect of spatial resolution on decoding accuracy in fMRI multivariate pattern analysis. NeuroImage 132, 32–42. https://doi.org/10.1016/j.neuroimage.2016.02.033.

Guntupalli, JS, Hanke, M, Halchenko, YO, Connolly, AC, Ramadge, PJ, Haxby, JV., 2016. A model of representational spaces in human cortex. Cereb. Cortex 26, 2919–2934.

Häusler, CO, Hanke, M., 2021. A studyforrest extension, an annotation of spoken language in the German dubbed movie "Forrest Gump" and its audio-description. F1000Research 10.

Huber, L, Finn, ES, Handwerker, DA, Bönstrup, M, Glen, DR, Kashyap, S, Ivanov, D, Petridou, N, Marrett, S, Goense, J., 2020. Sub-millimeter fMRI reveals multiple topographical digit representations that form action maps in human motor cortex. Neuroimage 208, 116463.

Huber, L, Handwerker, DA, Jangraw, DC, Chen, G, Hall, A, Stüber, C, Gonzalez-Castillo, J, Ivanov, D, Marrett, S, Guidi, M., 2017. High-resolution CBV-fMRI allows mapping of laminar activity and connectivity of cortical input and output in human M1. Neuron 96, 1253–1263.

Huber, LR, Poser, BA, Bandettini, PA, Arora, K, Wagstyl, K, Cho, S, Goense, J, Nothnagel, N, Morgan, AT, van den Hurk, J., 2021. LayNii: a software suite for layer-fMRI. Neuroimage 237, 118091.

In, M-H, Posnansky, O, Speck, O., 2016. PSF mapping-based correction of eddy-current-induced distortions in diffusion-weighted echo-planar imaging. Magn. Reson. Med. 75, 2055–2063.

Kassraian P, Rabe F, Maathuis M, Wenderoth N. 2022. Prior information improves tactile representation in primary somatosensory cortex. doi:10.1101/2022.10.10.511201.

Kilmarx, J, Oblak, E, Sulzer, J, Lewis-Peacock, J., 2021. Towards a common template for neural reinforcement of finger individuation. Sci. Rep. 11, 1065. https://doi.org/10.1038/s41598-020-80166-8.

Knights, E, Morcom, AM, Henson, RN., 2021. Does hemispheric asymmetry reduction in older adults in motor cortex reflect compensation? J. Neurosci. 41, 9361–9373. https://doi.org/10.1523/JNEUROSCI.1111-21.2021.

Kuehn, E, Dinse, J, Jakobsen, E, Long, X, Schäfer, A, Bazin, P-L, Villringer, A, Sereno, MI, Margulies, DS., 2017. Body topography parcellates human sensory and motor cortex. Cereb. Cortex 27, 3790–3805. https://doi.org/10.1093/cercor/bhx026.

Kuehn, E, Haggard, P, Villringer, A, Pleger, B, Sereno, MI., 2018. Visually-driven maps in area 3b. J. Neurosci. 38, 1295–1310. https://doi.org/10.1523/JNEUROSCI.0491-17.2017.

Kuehn, E, Pleger, B., 2020. Encoding schemes in somatosensation: from micro-to meta-topography. NeuroImage 223, 117255.

Liu, P, Chrysidou, A, Doehler, J, Hebart, MN, Wolbers, T, Kuehn, E, 2021. The organizational principles of de-differentiated topographic maps in somatosensory cortex. eLife 10, e60090. https://doi.org/10.7554/eLife.60090.

Lund, JS, Angelucci, A, Bressloff, PC., 2003. Anatomical substrates for functional columns in macaque monkey primary visual cortex. Cereb. Cortex 13, 15–24. https://doi.org/10.1093/cercor/13.1.15.

Mazziotta, J, Toga, A, Evans, A, Fox, P, Lancaster, J, Zilles, K, Woods, R, Paus, T, Simpson, G, Pike, B., 2001. A probabilistic atlas and reference system for the human brain: International Consortium for Brain Mapping (ICBM). Philos. Trans. R. Soc. London Ser. B Biol. Sci. 356, 1293–1322.

Pfannmöller, JP, Greiner, M, Balasubramanian, M, Lotze, M., 2016. High-resolution fMRI investigations of the fingertip somatotopy and variability in BA3b and BA1 of the primary somatosensory cortex. Neuroscience 339, 667–677.

Pleger, B, Wilimzig, C, Nicolas, V, Kalisch, T, Ragert, P, Tegenthoff, M, Dinse, HR., 2016. A complementary role of intracortical inhibition in age-related tactile degradation and its remodelling in humans. Sci. Rep. 6, 27388. https://doi.org/10.1038/srep27388.

Ruitenberg, MFL, Cassady, KE, Reuter-Lorenz, PA, Tommerdahl, M, Seidler, RD., 2019. Age-related reductions in tactile and motor inhibitory function start early but are independent. Front. Aging Neurosci. 11.

Sabuncu, MR, Singer, BD, Conroy, B, Bryan, RE, Ramadge, PJ, Haxby, JV., 2010. Function-based intersubject alignment of human cortical anatomy. Cereb. Cortex 20, 130–140.

Schweisfurth, MA, Schweizer, R, Treue, S., 2014. Feature-based attentional modulation of orientation perception in somatosensation. Front. Hum. Neurosci. 8, 519.

Schweizer, R, Braun, C, Fromm, C, Wilms, A, Birbaumer, N., 2001. The distribution of mislocalizations across fingers demonstrates training-induced neuroplastic changes in somatosensory cortex. Exp. Brain Res. 139, 435–442.

Sereno, MI, Dale, AM, Reppas, JB, Kwong, KK, Belliveau, JW, Brady, TJ, Rosen, BR, Tootell, RB., 1995. Borders of multiple visual areas in humans revealed by functional magnetic resonance imaging. Science 268, 889–893. https://doi.org/10.1126/science.7754376.

Turek, JS, Ellis, CT, Skalaban, LJ, Turk-Browne, NB, Willke, TL., 2018. Capturing shared and individual information in fMRI data. In: 2018 IEEE International Conference on Acoustics, Speech and Signal Processing (ICASSP). IEEE, pp. 826–830.
Yacoub, E, Harel, N, Uğurbil, K., 2008. High-field fMRI unveils orientation columns in humans. Proc. Natl. Acad. Sci. 105, 10607–10612.
Yang, J, Huber, L, Yu, Y, Chai, Y, Khojandi, A, Bandettini, PA., 2019. High-resolution fMRI maps of columnar organization in human primary somatosensory cortex. In: Proc. Int. Soc. Mag. Reson. Med., p. 0617.